ENVIRONMENTAL STUDIES

# Satellite-based survey of extreme methane emissions in the Permian basin

**Itziar Irakulis-Loitxate[1†], Luis Guanter[1*†], Yin-Nian Liu[2*], Daniel J. Varon[3,4], Joannes D. Maasakkers[5], Yuzhong Zhang[6,7], Apisada Chulakadabba[3], Steven C. Wofsy[3], Andrew K. Thorpe[8], Riley M. Duren[8,9], Christian Frankenberg[8,10], David R. Lyon[11], Benjamin Hmiel[11], Daniel H. Cusworth[8], Yongguang Zhang[12], Karl Segl[13], Javier Gorroño[1], Elena Sánchez-García[1], Melissa P. Sulprizio[3], Kaiqin Cao[2], Haijian Zhu[2], Jian Liang[2], Xun Li[2], Ilse Aben[5], Daniel J. Jacob[3]**



**Industrial emissions play a major role in the global methane budget. The Permian basin is thought to be responsible for almost half of the methane emissions from all U.S. oil- and gas-producing regions, but little is known about individual contributors, a prerequisite for mitigation. We use a new class of satellite measurements acquired during several days in 2019 and 2020 to perform the first regional-scale and high-resolution survey of methane sources in the Permian. We find an unexpectedly large number of extreme point sources (37 plumes with emission rates >500 kg hour$^{-1}$), which account for a range between 31 and 53% of the estimated emissions in the sampled area. Our analysis reveals that new facilities are major emitters in the area, often due to inefficient flaring operations (20% of detections). These results put current practices into question and are relevant to guide emission reduction efforts.**

## INTRODUCTION

Methane ($CH_4$) is the second most important anthropogenic greenhouse gas and a precursor for tropospheric ozone, which acts as both greenhouse gas and air pollutant. Due to methane's strong radiative forcing potential and its short lifetime in the atmosphere (9±1 years) (*1*), the reduction of methane emissions is being prioritized as an effective climate change mitigation measure on decadal time scales (*2*).

Methane levels in the atmosphere have almost tripled since preindustrial times (*3*). Along with agriculture, oil and natural gas (O&G) production operations are one of the primary causes for this increase, but the magnitude, dynamics, spatial distribution, and driving mechanisms of methane emissions from O&G production remain poorly understood. This is especially concerning for the United States, which is the world leader in O&G production, owing to its rapid growth in the last two decades. Alvarez *et al.* (*4*) estimated that 13 Tg $CH_4$ a$^{-1}$ was emitted from the U.S. national O&G supply chain in 2015, which is 78% higher than the most recent estimates by the U.S. Environmental Protection Agency (EPA) for that year, and represents an important fraction of the 68- to 92-Tg $CH_4$ a$^{-1}$ range estimated globally for upstream and downstream O&G sectors in the 2008–2017 decade (*5*). This large share of methane emissions from the U.S. O&G sector is increasing. For example, Jackson *et al.* (*6*) reported that fossil fuel–related methane emissions in the United States increased between 3.4 and 4.0 Tg $CH_4$ a$^{-1}$ from 2000–2006 to 2017, which is approximately 80% of the total increase of methane emissions for North America in that period.

Methane emissions from O&G production originate mainly from point sources including wells, gathering stations, compressor stations, storage tanks, pipelines, processing plants, and flares. There may be thousands of these individual point sources in a typical O&G field (*7*). A small fraction of facilities are responsible for a large share of total emissions at any given time, which may be caused by intentional venting of wells and storage tanks, inefficient flaring, or leaks from malfunctioning equipment (*7*). O&G production in the Permian basin, located in New Mexico and Texas, has been growing rapidly over the past decade, and the Permian is now the largest O&G-producing basin in the United States. This was covered by a recent study by Zhang *et al.* (*8*), which combined satellite observations from the Tropospheric Monitoring Instrument (TROPOMI) onboard the Sentinel-5P satellite with atmospheric modeling methods to find Permian methane emissions from O&G production to be 2.7±0.5 Tg $CH_4$ a$^{-1}$. This number represents the largest methane flux ever reported from a U.S. O&G-producing region; it is more than twice the bottom-up estimates for the Permian, and a factor of 4 higher than estimates for any other Unites States O&G basin.

Better characterizing the nature, intensity, and dynamics of methane point emissions from the world's O&G basins, and in particular from the Permian, is not only critical to close the gap between bottom-up and top-down anthropogenic emission estimates but also to facilitate emission reductions. Better emission characterization is also crucial for understanding the contribution of the O&G production sector to the acceleration of the methane growth rate in the atmosphere. Airborne measurement methods, through either mass balance (*9*, *10*) or imaging spectroscopy (*11*–*16*), are a powerful approach to detect and monitor methane point sources

[1]Research Institute of Water and Environmental Engineering (IIAMA), Universitat Politècnica de València (UPV), Valencia, Spain. [2]CAS Key Laboratory of Infrared System Detection and Imaging Technology, Shanghai Institute of Technical Physics, Shanghai, China. [3]School of Engineering and Applied Sciences, Harvard University, Cambridge, MA, USA. [4]GHGSat Inc., Montréal, Quebec, Canada. [5]SRON Netherlands Institute for Space Research, Utrecht, Netherlands. [6]Key Laboratory of Coastal Environment and Resources of Zhejiang Province (KLaCER), School of Engineering, Westlake University, Hangzhou, Zhejiang, China. [7]Institute of Advanced Technology, Westlake Institute for Advanced Study, Hangzhou, Zhejiang, China. [8]Jet Propulsion Laboratory, California Institute of Technology, Pasadena, CA, USA. [9]University of Arizona, Tucson, AZ, USA. [10]California Institute of Technology, Pasadena, CA, USA. [11]Environmental Defense Fund, Austin, TX, USA. [12]International Institute for Earth System Sciences, Nanjing University, Nanjing, China. [13]Helmholtz Center Potsdam, GFZ German Research Center for Geosciences, Potsdam, Germany.
*Corresponding author. Email: lguanter@fis.upv.es (L.G.); ynliu@mail.sitp.ac.cn (Y.-N.L.)
†These authors contributed equally to this work.

over large O&G regions. In particular, so-called imaging spectrometers offer a unique observational configuration to map methane point emissions with simultaneously high accuracy and spatial sampling. These instruments produce images of the solar radiation reflected by the Earth surface at hundreds of wavelengths, including those in the shortwave infrared region of the electromagnetic spectrum sampling the strong methane absorption band around 2300 nm (see fig. S1). High-resolution maps of methane plumes (up to 3 to 4 m for airborne instruments) can be inferred from these observed spectra using atmospheric retrieval techniques (see Materials and Methods).

Satellite remote sensing represents a critical means for systematic monitoring of point emissions from O&G-producing regions around the world (*17*). The Sentinel-5P/TROPOMI mission, launched in 2017, is a crucial step toward the monitoring of methane emissions from space (*18*–*21*), but its 7-km pixel size does not generally allow sampling of individual point sources (*22*). Instead, high-resolution (~30-m) methane retrievals can be performed using satellite imaging spectrometers (*23*), which trade TROPOMI's fine spectral resolution for fine spatial resolution. This trade-off does not allow retrieval of small methane sources but is ideal for detecting large point sources, as demonstrated with the EO-1/Hyperion during the Aliso Canyon methane blowout (*24*). The GHGSat-D private satellite has also shown capability of retrieving large methane sources at 50-m spatial resolution (*25*, *26*).

In this study, we take advantage of the rapid development of spaceborne imaging spectroscopy technology and data processing methods to perform the first satellite-based large-scale and high-resolution survey of methane point emitters in the Permian basin. Our dataset was acquired by three satellite missions launched between 2018 and 2019: two versions of the Advanced Hyperspectral Imager (AHSI) onboard China's Gaofen-5 (GF5) and ZY1 satellites (*27*) and the imaging spectrometer onboard Italy's PRISMA mission (see Materials and Methods). We cover a ~150 km–by–200 km area in the Delaware sub-basin of the Permian basin with a total of 30 images acquired within several days, but mostly on four different dates: 15 May 2019, 1 November 2019, 29 December 2019, and 8 February 2020 (see table S1 and fig. S2). We generate maps of methane concentration enhancements ($\Delta CH_4$), from which we detect methane plumes through visual inspection (fig. S3). We calculate emission flux rates ($Q$) for each plume using the integrated methane enhancement (IME) method and large eddy simulations performed specifically for our satellite observations (fig. S4). See Materials and Methods for further information on the derivation of methane plumes and the conversion to emission rates. We evaluated the sensitivity of our satellite measurements to methane enhancements and the uncertainties in methane flux calculation by means of simulation-based studies (texts S1 and S2 and figs. S5 to S8). The 30-m spatial sampling of our survey allows us to map individual methane plumes and to attribute emissions to specific infrastructure. Our core objective is to identify, characterize, and quantify the largest point emissions in the area, with the overarching motivation of assisting future emission reduction efforts.

## RESULTS

### Imaging extreme methane point sources

Figure 1 shows the location and intensity of the 37 methane plumes that we have detected over the Delaware sub-basin of the Permian after the processing of our satellite imaging spectroscopy dataset. The detected point emissions have $Q$ typically between 500 kg hour$^{-1}$ (which we assume as both our detection limit and our definition of an "extreme emission") and 6000 kg hour$^{-1}$. Most plumes are located in the 31.0° to 32.5°N, 103.3° to 104.2°W subregion. This matches the area of highest methane fluxes revealed by top-down estimates by Zhang *et al.* (*8*) but is less well aligned with the bottom-up emission inventory based on the U.S. EPA greenhouse gas inventory (*28*) updated to account for 2018 infrastructure using well-level information from Enverus DrillingInfo (fig. S9) (*29*).

Subpanels around the main panel of Fig. 1 show examples of individual methane plumes (see table S1 and fig. S10 for details on plume locations, intensity, and type of emitting facility). There is a relatively large variability in both emission rates and source types. For example, plume a corresponds to a large emission ($Q$ = 3590±1220 kg hour$^{-1}$) from an area devoid of visible infrastructure elements such as well pads and storage tanks; plume b ($Q$ = 2119±608 kg hour$^{-1}$) is associated with the incomplete combustion of a flare from a tank battery; plume f is a strong emission ($Q$ = 4385±1296 kg hour$^{-1}$) that we attribute to the venting of a gas well; plumes g and j are two very large emissions ($Q$ of 5952±2556 and 5472±2159 kg hour$^{-1}$, respectively) from compression stations. Last, plume c is a special case. It corresponds to an emission of an abnormally high magnitude ($Q$ = 18,492±6570 kg hour$^{-1}$) from an unknown source. The absence of correlation between the spatial distribution of the methane enhancement and surface brightness and composition indicates that this is a real methane plume and not the result of a processing artifact (see fig. S11 for maps of the surface and its mineralogy) (*30*). We attribute it to a large transient release, potentially from one of the large natural gas gathering pipelines in the area. A strong methane enhancement is seen by TROPOMI at the same location in the days around this event (fig. S12), but we are not able to determine what fraction of the enhancement is actually due to this particular emission.

We do not find multiple plume detections from any of the methane sources in our satellite dataset, which may be due to the relatively high detection limit of our measurements (~500 kg hour$^{-1}$, see text S1) and the limited temporal sampling of our data: 32 of 37 plumes are derived from four different overpasses between 15 May 2019 and 8 February 2020, with 19 of them corresponding to the same GF5-AHSI overpass (see table S1 and fig. S2). However, we do find correspondence between our detections and highly accurate $\Delta CH_4$ maps from an independent airborne AVIRIS-NG imaging spectrometer campaign sampling over some areas in the Permian included in our large-scale satellite survey (see fig. S13 for examples).

### Strength of point emissions in the Permian basin

The distribution of flux rates from all the detected emissions in the Permian is shown in Fig. 2. Of 37 detected plumes, 29 have fluxes larger than 1000 kg hour$^{-1}$. To our knowledge, the Delaware sub-basin of the Permian therefore contains the highest number of extreme point emitters ever observed across a single O&G-producing basin. For example, the magnitude of the emission rates in the Permian is substantially higher than the one previously cataloged in the Barnett Shale basin, where only 5 of 17,400 well pads were found to emit more than 300 kg hour$^{-1}$ (*31*, *32*). Moreover, only seven emissions larger than 1000 kg hour$^{-1}$ were found over the Four Corners natural gas–producing region from a total of 250 plumes identified during a comprehensive campaign using the AVIRIS-NG airborne

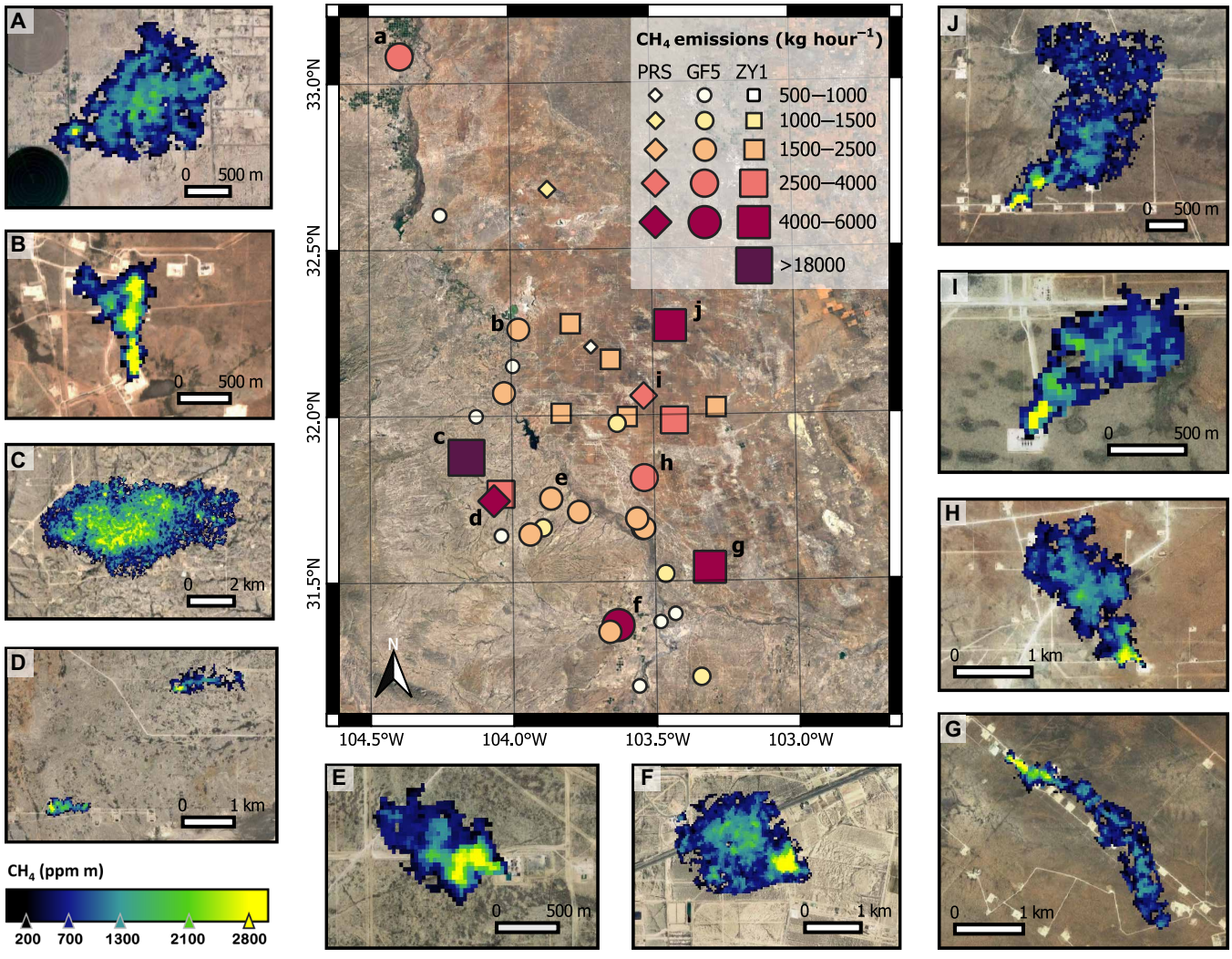


**Fig. 1. Extreme methane emissions detected in the Permian basin from satellite imaging spectroscopy data.** A map with the identified methane plumes is shown in the central panel. Emissions are coded according to their flux rate and to the source of data (GF5-AHSI, GF5; ZY1-AHSI, ZY1; PRISMA, PRS). The small panels (A to J) around the main figure show examples of the detected plumes.

imaging spectrometer, which is similar to the satellite instruments used in this study (*14*). It must be noted, though, that the area sampled by airborne instruments in the Four Corners region was also smaller (~60 km by 50 km) than the one we have been able to cover in the Permian basin with satellite imaging spectrometers (~150 km by 200 km). This implies that it is the total number of extreme emitters, and not the spatial density of sources, that makes the Permian to be such an outstanding case.

Despite the fact that some of the emissions detected at Four Corners are due to coal mine vents rather than to O&G extraction facilities, we consider the Four Corners dataset as the best reference for our Permian survey, as their use of airborne imaging spectrometers to detect and quantify emissions inherently leads to a systematic survey of high point emitters. Integrated emission estimates for the two regions are shown in the inset of Fig. 2. The emission rate reported for Four Corners corresponds to the sum of all ~250 plumes detected from the dataset collected in the airborne campaign, for which a detection limit of ~2 to 5 kg hour$^{-1}$ was estimated (*14*). In the case of the Permian basin, we consider only the 19 plumes detected from one single overpass of the GF5-AHSI system on 8 February 2020, as GF5-AHSI has the highest sensitivity and measurement accuracy (see text S1 and figs. S5 and S6). The flux rates estimated for those 19 plumes are aggregated and scaled from per-hour to per-year units for direct comparison with the per-year amounts given by Frankenberg *et al.* (*14*) for Four Corners. The resulting integrated flux from the Permian plumes is 0.28 Tg a$^{-1}$ (0.20 to 0.35 Tg a$^{-1}$ 95% confidence interval), which is close to the 0.3 Tg a$^{-1}$ (0.23 to 0.39 Tg a$^{-1}$ 95% confidence interval) reported for Four Corners, despite the much smaller number of plumes detected from our satellite data. Although our total emission rate and its confidence interval are calculated from a small dataset, we estimate them to have a 1-σ uncertainty below 13% (see text S3 and fig. S14). This simple comparison with the Four Corners dataset illustrates the outstanding strength of the methane emissions currently occurring in the Permian basin. Measurement differences between the two datasets (most important, spatial resolution and detection limit) prevent a more detailed analysis.

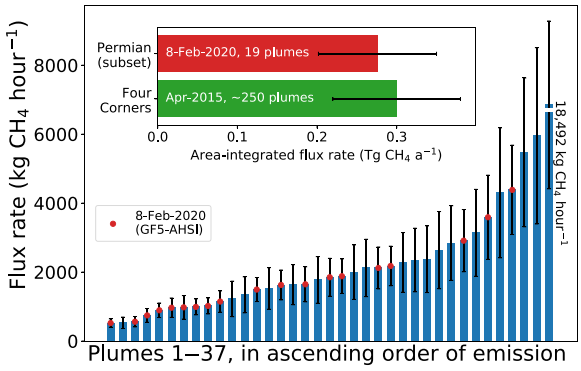


**Fig. 2. Distribution of emission rates for the 37 methane plumes detected over the Permian basin with satellite imaging spectroscopy.** The last bar corresponds to the massive emission displayed in Fig. 1C, whose flux rate exceeds the plot range. The inset plot shows a comparison of area-wide flux estimates from the integration of single emissions detected over the Permian on 8 February 2020 by the GF5-AHSI system (emissions marked as red circles in the main plot) and over the Four Corners region during the April 2015 AVIRIS-NG airborne campaign described in (*14*). Vertical error bars correspond to 1-σ precision errors in flux rate calculations, and horizontal error bars correspond to the 95% confidence interval in areal flux estimates calculated through bootstrapping for the two datasets.

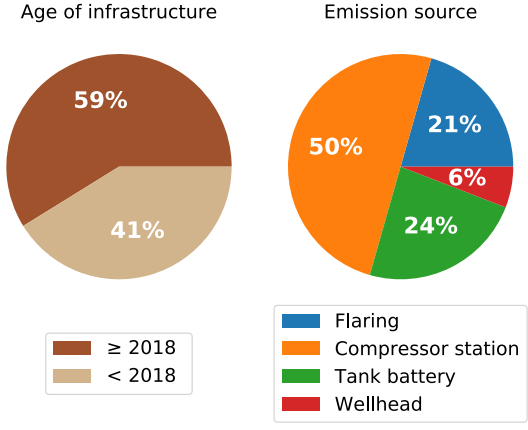


**Fig. 3. Breakdown of satellite-detected extreme methane emissions (>500 kg hour$^{-1}$) over the Permian basin.** Emissions are classified in terms of the year in which the infrastructure started production (left) and of the emission source (right). The data represent the percentage of plumes detected in each category as a function of the total number of plumes for which source information was available.

We have also compared our detected point emissions with area-integrated emission estimates generated through top-down inversions of TROPOMI satellite concentrations using the method described by Zhang *et al.* (*8*). This comparison of single-point emissions with area-integrated emissions is only intended to provide further context for the magnitude of the extreme point emissions that we have detected. Top-down area integrated emission estimates give 0.73 Tg a$^{-1}$ for the Permian area sampled by GF5-AHSI on 8 February 2020 on the basis of a February 2020 (monthly) inversion run. The single point emissions sampled by GF5-AHSI on 8 February 2020 represent then a 38% (31 to 53% confidence interval) of that areal emission. This "tail-heavy" nature of O&G methane emission distributions has been previously reported (*4*, *33*). For example, our numbers are roughly consistent with a 2015 Barnet Shale inventory, which found that fat-tailed emissions made up 19% of regional O&G emissions (*31*), whereas >500–kg hour$^{-1}$ emissions represented about 50% of the total 2015 Four Corners emission rate from point sources (*14*). Our plume detections only represent snapshots in time of those emissions with an intensity higher than 500 kg hour$^{-1}$ at the time of the satellite overpass, and our scaling from per-hour to per-year units is done for comparison on a common basis. Because most of the emissions are intermittent, we assume that the detected sources provide a statistical sampling of large emitters on the regional level to scale up to a representative annual estimate.

## Breakdown of emission sources

The high spatial resolution of our data allows us to directly attribute the detected plumes to specific infrastructure (see Materials and Methods and fig. S15). A breakdown of the characteristics of the 34 plumes for which information on the emitting infrastructure could be found is presented in Fig. 3 (see table S1 for more details). We classify emissions in terms of the emission source (flaring, compressor station, tank battery, or wellheads) and the age of the emitting infrastructure.

The first important result from this analysis is that we detect more extreme emissions from facilities starting production in 2018 or later than from older ones, irrespective of whether we base the calculation on the number of detected plumes (59 to 41%) or on the amount of methane emitted by them (51 to 49%). This is unexpected if we take into consideration that the number of wells producing before 2018 represents 65% of active wells in our study area (see Materials and Methods). According to these numbers, extreme emissions occur 2.6 times more frequently for new facilities (those from 2018 or after) than from old facilities, and the amount of methane emitted by new facilities is twice the one emitted from the older ones. This finding agrees with the results from a large helicopter-based emission survey over seven U.S. basins, which found that well pads in their first 2 months of production were five times more likely to have detected emissions (*7*). This result supports the speculation that recently developed wells and infrastructure associated with these wells are the major methane emitters in the Permian basin (*8*), which is likely due to a faster development of gas extraction methods than of storage and processing capabilities. We do not rule out the possible contribution of exploratory drilling to these large emissions from new facilities, as uncontrolled methane emissions during the drilling of new wells can be large.

Second, we find a surprisingly high share of emissions (21%, in terms of both number of plumes and amount of emitted methane) from active flaring processes (see fig. S15 for an example of a large methane plume being emitted during flaring). The flux rates of the detected emissions from flaring are between 1640 and 2640 kg hour$^{-1}$ (see table S1). Although this range is in the lower half of our emission distribution (Fig. 2), such high emission rates can only be explained by inefficient or malfunctioning flaring operations (*7*, *34*). This finding agrees with a study in the Bakken Shale, which estimated that incomplete combustion from flares contributed almost 20% of the total field emissions of methane, most of which was due to a small number of low-efficiency flares (*35*). We note that all seven detected flaring-related emissions are from new well pads and

tanks, namely, one infrastructure element from 2017, four from 2018, and two from 2019 (see table S1). This reinforces the hypothesis that the higher extraction potential of new infrastructure might not be matched by an equal development in gathering, processing, and transportation facilities.

## DISCUSSION

Our space-based high-resolution mapping approach has enabled a first large-scale survey of methane point emitters in the Permian basin, one of the top O&G-producing regions of the world. The 30-m resolution and wide area coverage of the newly developed satellite technology used in this work has proven to be an effective means to detect, quantify, and classify strong methane point emissions. From satellite data acquired during several days in 2019 and 2020, we find a large number of extreme point sources, with flux rates typically ranging from 500 to 6000 kg hour$^{-1}$ and a recent massive emission of >18,000 kg hour$^{-1}$. Our analysis of emission sources reveals that new facilities (starting production in 2018 or later) are major emitters, which could be caused by a limited ability of storage, processing, and transportation facilities to cope with the high production of unconventional wells. This is supported by the high fraction of emissions from flaring (21%, all of them from new wells), as it has recently been reported in mass media (*36*). This finding has strong implications for the design and regulation of O&G production activities in the Permian basin, and could be extrapolated to other O&G-producing regions.

We have demonstrated that spaceborne high-resolution imaging spectroscopy has a great potential for both operational surveillance of fugitive or unpermitted emissions from O&G activities and for the improvement of bottom-up emissions inventories. However, further work is needed on both spaceborne imaging spectrometer technology and data processing methods to lower the 500 kg hour$^{-1}$ detection limit that we estimate for our data and to improve spatial and temporal coverage. A number of satellite high-resolution imaging spectroscopy missions with similar characteristics to the ones used in this work will be launched in the next years. These include, first, a new version of the GF5-AHSI system, the German EnMAP mission (*37*), and NASA's EMIT, planned for launch in the next couple of years, and, later, European Space Agency's (ESA's) CHIME and NASA's SBG missions in the 2025–2030 time frame. The latter two will combine a high measurement sensitivity, a global coverage at 30-m sampling, a 2- to 3-week revisit time, and an open data policy. In combination with TROPOMI's daily revisit and high-accuracy measurements, to be soon complemented by the upcoming MethaneSAT mission, high-resolution imaging spectroscopy missions have a strong promise for operational, unbiased, open-access, and cost-effective monitoring of methane point sources. It can be anticipated that this global scenario for high-resolution methane mapping will be complemented by private satellite missions, of which the GHGSat-D mission is currently the best example, and by multispectral missions with spectral coverage of the 2300-nm spectral feature such as Sentinel-2, sensitive to large methane emissions over spatially homogeneous targets (*38*).

Our results suggest that the rapid installation of new O&G production facilities in the Permian basin might not be counterbalanced by sufficient parallel development of gas gathering and processing infrastructure, which would lead to a high concentration of extreme emissions in the region due to issues such as unlit associated gas flares (*39*). This situation could be affected by environmental regulations, which have been recently weakened at the federal level (*40*). We argue that satellite-based methods are valuable to detect and monitor potential changes in methane point emissions in O&G-producing regions, which will also enable the industry to efficiently reduce emissions by identifying and repairing problems causing extreme, but sometimes intermittent, emissions that are often unnoticed by traditional leak detection approaches.

## MATERIALS AND METHODS

### Satellite imaging spectroscopy data

Imaging spectroscopy, also known as hyperspectral imaging, is a remote sensing technique in which images of the solar radiation reflected by the Earth are produced in hundreds of spectral channels between the visible and the shortwave infrared part of the electromagnetic spectrum (roughly 400 to 2500 nm). This dense spectral sampling enables the use of spectroscopic techniques to detect and quantify the Earth's surface and atmosphere constituents based on their spectral signatures.

We use data from three new hyperspectral satellite missions, each one carrying an imaging spectrometer as payload. These are two versions of the AHSI onboard the GF5 and ZY1 platforms (China, launched in May 2018 and September 2019, respectively) (*27*) and the core instrument onboard PRISMA (Italy, launched in March 2019). These instruments sample the 400- to 2500-nm spectral window with a pixel size of 30 m. AHSI images cover an area of 60 km by 60 km, whereas PRISMA images cover areas of 30 km by 30 km. Measurements in the short-wave infrared spectral region from 2000 to 2500 nm sample absorption features from water vapor, carbon dioxide, and methane. The 2100- to 2450-nm window is especially sensitive to methane (see fig. S1) and is therefore the one we use for our methane retrievals.

In our study, we have combined a total of 30 images acquired from all three systems to cover a 150 km–by–200 km area in the Permian basin (see fig. S2). These missions are operated through sporadic pointing at selected targets, so they do not acquire data systematically over every single point on Earth (as opposed to global coverage missions such as TROPOMI). The acquisitions used in this work were mostly taken between May 2019 and August 2020, and most of the detections are from images acquired on four different days (15 May 2019 and 8 February 2020 for GF5-AHSI, and 1 November 2019 and 29 December 2019 for ZY1 AHSI) (see table S1). In particular, 19 plumes were detected from a single overpass of GF5-AHSI on 8 February 2020.

### Retrieval of methane concentration enhancements

We calculate methane concentration enhancements (i.e., increments above background levels in the amount of methane present in the atmospheric column, $\Delta CH_4$) using a so-called matched filter image processing technique applied to spectra in the 2110- to 2450-nm spectral fitting window. Matched filter methods have been widely tested for methane retrieval from airborne imaging spectroscopy data (*12*, *41*) and on one occasion with spaceborne data (*24*). These methods seek to detect a target spectrum (in our case, a methane absorption spectrum) across a hyperspectral image using statistics extracted from the data. We use radiative transfer simulations to generate a unit absorption spectrum, which represents the change in radiance for a 1-ppm (part per million) increase in methane

concentration over a pathlength of 1 m. The matched filter uses this unit absorption spectrum to convert changes in radiance into $\Delta CH_4$ in ppm·m units. Assuming a scale height of 8 km, 10,000 ppm·m translate to a $\Delta CH_4$ of 1.25 ppm (*24*). The statistics needed by the matched filter (mean spectrum and covariances) are calculated on a per-column basis to account for across-track changes in the instrument's radiometric and spectral response usually occurring in imaging spectrometers. The retrieval is run for all pixels of the image to produce $\Delta CH_4$ maps with a 30-m sampling.

We have evaluated the performance of the matched filter retrieval with our satellite data through a simulation-based sensitivity analysis optimized for the Permian conditions. Details are provided in text S1. From this analysis, we conclude that the retrieval is not biased, that GF5-AHSI is substantially more sensitive to $\Delta CH_4$ than ZY1-AHSI and PRISMA, and that representative $\Delta CH_4$ 1-σ precision errors are 63, 101, and 149 ppb (parts per billion) for GF5-AHSI, ZY1-AHSI, and PRISMA, respectively (figs. S5 and S6).

### Estimation of emission rates from methane concentration enhancement maps

From the resulting $\Delta CH_4$ maps, we detect emission plumes through visual inspection of the data. We search for methane enhancements within the image with the typical shape of a gas plume from a point emitter (i.e., higher concentrations at the source and progressive decrease downwind). We compare the plume direction with that of the wind as further evidence to conclude that the enhancement is from a real emission and not a retrieval artifact.

For each of the detected plumes, we apply a 200-ppm·m threshold to define the background signal and manually define a polygon to mask it out from the background (see fig. S3). With the pixels included in the plume mask, we calculate an IME as the total mass of methane contained in the plume (*14*). The IME is typically expressed in kilograms and represents the total mass of excess methane within the plume structure. After Varon *et al.* (*42*), we link the IME to the emission flux rate $Q$ as

$$Q = \frac{U_{\text{eff}} \cdot \text{IME}}{L} \quad (1)$$

where $U_{\text{eff}}$ is an effective wind speed and $L$ is the plume length scale (square root of the plume mask area). For the calculation of $U_{\text{eff}}$, we use large eddy simulations to establish the following empirical relationships between $U_{\text{eff}}$ and the measurable 10-m wind speed $U_{10}$ (see fig. S4)

$$U_{\text{eff}} = 0.34 \cdot U_{10} + 0.44 \quad (2)$$

These simulations were specifically performed for a spatial resolution and measurement uncertainty compatible with our data using the methodology described by Varon *et al.* (*42*). Our processing takes $U_{10}$ data from the GEOS-FP dataset for the time and location of each detected plume.

### Assessment of uncertainties in the estimated emission rates

For the estimation of the associated flux rate uncertainties, we have implemented an uncertainty propagation formalism similar to the one proposed by Cusworth *et al.* (*16*). We assume errors in the input 10-m wind speed $U_{10}$ and the IME derived from the $\Delta CH_4$ maps. We choose a conservative 50% uncertainty estimate in GEOS-FP $U_{10}$ data consistent with the ~1.5-m/s error SD in wind speed given by Varon *et al.* (*26*). A random distribution of $U_{10}$ values is generated around the actual GEOS-FP $U_{10}$ value for each plume. A distribution of $Q$ values is calculated for each plume from the $U_{10}$ distribution using Eqs. 1 and 2 with the actual values of IME and $L$. The SD of the resulting $Q$ ensemble is taken as the precision error (1-σ) of the estimated flux for each plume.

The resulting absolute and relative 1-σ uncertainties for the 37 plumes detected in this study are presented in fig. S7. Relative precision errors are in the range of 20 to 45% and are strongly dominated by the contribution of $U_{10}$ uncertainties on the flux calculation (~18 to 40%), whereas uncertainties from retrieval noise in the IME calculation are typically between 2 and 7%. The ranges for the uncertainty contributions from wind and retrieval noise are roughly consistent with the study by Varon *et al.* (*26*) for the GHGSat-D satellite (16 to 27% for the wind contribution and 7% for the retrieval, for a total error of 40 to 45%) despite the much finer spectral resolution of GHGSat-D than the imaging spectroscopy mission used in this study. Uncertainties in flux rate estimation from satellite imaging spectroscopy data were also analyzed by Cusworth *et al.* (*23*). They estimated a relative random error in the range of 15 to 25% for bright surfaces such as in the Permian, although the absolute flux rates were underestimated by ~35% in the case of a bright surface and 900 kg hour$^{-1}$ source, which is the closest scenario to the observation conditions of our Permian study. According to the authors, one of the causes for this underestimation could be the fact that the $U_{10} - U_{\text{eff}}$ relationship was not explictly derived for the spatial resolution and retrieval sensitivity of the imaging spectroscopy missions under evaluation, which is not the case in our study.

The magnitude of our estimated plume-level emission rates has been further assessed through a simulation-based study with the Weather Research Forecast model version 3.9.1 coupled with Chemistry in Large Eddy Simulation mode (WRF-Chem-LES) (*43*). Three of the observed plumes (k, l, and x) have been simulated with WRF-Chem-LES and wind data from National Oceanic and Atmospheric Administration's High-Resolution Rapid Refresh (HRRR) model. The results from this analysis confirm the extreme magnitude of the estimated $Q$ as well as the validity of our precision error estimates derived from the propagation of wind uncertainties. On the other hand, this analysis has revealed that assumptions of the IME-based $Q$ estimation model, not included in our precision error estimates, can also represent an important source of uncertainty. See text S2, fig. S8, and table S2 for further details.

### Attribution of plumes to emitting infrastructure elements

The 30 m–by–30 m spatial sampling of our satellite imaging spectroscopy data enables the identification of methane point sources (see fig. S15), even within oil and gas extraction platforms, and storage tank or compressor station platforms, which have a typical size between 60 and 600 m$^2$ in the Permian. We use high-resolution Google Earth (GE) images co-registered with the methane enhancement maps to attribute sources to emissions. Sentinel-2 10-m images were used instead of GE images in those cases in which the GE data were not available for the time and location of the detected methane plume.

Some details on platform type (oil or gas well or tank battery), extraction start year, and status (active/inactive) have been collected from the interactive PermianMAP (*44*) of the Environmental Defense Fund (EDF), which offers data generated by the Railroad Commission of Texas (*45*) and New Mexico's Department of Energy, Minerals, and Natural Resources (*46*). Other data not available in

PermianMAP have been obtained through visual interpretation of the satellite images and the information provided by the Sentinel-2 historical record. Using this information, we can identify the emission source of most of the detected plumes, being these compressor stations, tank batteries, wellheads, or emissions derived from flaring. The latter are easily identified by the high signal emitted by the torch flame at ~2300 nm (*34*) and by the location of the plume above the chimney (see fig. S15).

Regarding the information on well age, we extracted well information from Enverus DrillingInfo (*29*) for all wells in New Mexico and Texas reporting production in 2020. We calculate statistics for wells in the region with most plume detections (31.0° to 32.5°N,103.3° to 104.2°W). In this count, the term "wells" refers to well pads that may contain multiple wells and infrastructure elements. To see when wells were finished, we use their month of first production as completion date. Because wells that have been active for a long time but hardly produce anymore (stripper wells) can skew the average, we also calculate mean well ages for the subset of wells with substantial production (defined as 10% of the mean production per well). The count has resulted in a total number of wells of 6993, with 4516 of them producing since before 2018 (65% of the total). The average year of start of production for these wells with substantial production in the area of interest is 2015.35.

## SUPPLEMENTARY MATERIALS

Supplementary material for this article is available at http://advances.sciencemag.org/cgi/content/full/7/27/eabf4507/DC1

## REFERENCES AND NOTES


1. M. J. Prather, C. D. Holmes, J. Hsu, Reactive greenhouse gas scenarios: Systematic exploration of uncertainties and the role of atmospheric chemistry. *Geophys. Res. Lett.* **39**, L09803 (2012).
2. D. Shindell, J. C. I. Kuylenstierna, E. Vignati, R. van Dingenen, M. Amann, Z. Klimont, S. C. Anenberg, N. Muller, G. Janssens-Maenhout, F. Raes, J. Schwartz, G. Faluvegi, L. Pozzoli, K. Kupiainen, L. Höglund-Isaksson, L. Emberson, D. Streets, V. Ramanathan, K. Hicks, N. T. K. Oanh, G. Milly, M. Williams, V. Demkine, D. Fowler, Simultaneously mitigating near-term climate change and improving human health and food security. *Science* **335**, 183–189 (2012).
3. B. Hmiel, V. V. Petrenko, M. N. Dyonisius, C. Buizert, A. M. Smith, P. F. Place, C. Harth, R. Beaudette, Q. Hua, B. Yang, I. Vimont, S. E. Michel, J. P. Severinghaus, D. Etheridge, T. Bromley, J. Schmitt, X. Faïn, R. F. Weiss, E. Dlugokencky, Preindustrial $^{14}CH_4$ indicates greater anthropogenic fossil $CH_4$ emissions. *Nature* **578**, 409–412 (2020).
4. R. A. Alvarez, D. Zavala-Araiza, D. R. Lyon, D. T. Allen, Z. R. Barkley, A. R. Brandt, K. J. Davis, S. C. Herndon, D. J. Jacob, A. Karion, E. A. Kort, B. K. Lamb, T. Lauvaux, J. D. Maasakkers, A. J. Marchese, M. Omara, S. W. Pacala, J. Peischl, A. L. Robinson, P. B. Shepson, C. Sweeney, A. Townsend-Small, S. C. Wofsy, S. P. Hamburg, Assessment of methane emissions from the U.S. oil and gas supply chain. *Science* **361**, 186–188 (2018).
5. M. Saunois, A. R. Stavert, B. Poulter, P. Bousquet, J. G. Canadell, R. B. Jackson, P. A. Raymond, E. J. Dlugokencky, S. Houweling, P. K. Patra, P. Ciais, V. K. Arora, D. Bastviken, P. Bergamaschi, D. R. Blake, G. Brailsford, L. Bruhwiler, K. M. Carlson, M. Carrol, S. Castaldi, N. Chandra, C. Crevoisier, P. M. Crill, K. Covey, C. L. Curry, G. Etiope, C. Frankenberg, N. Gedney, M. I. Hegglin, L. Höglund-Isaksson, G. Hugelius, M. Ishizawa, A. Ito, G. Janssens-Maenhout, K. M. Jensen, F. Joos, T. Kleinen, P. B. Krummel, R. L. Langenfelds, G. G. Laruelle, L. Liu, T. Machida, S. Maksyutov, K. C. McDonald, J. M. Norton, P. A. Miller, J. R. Melton, I. Morino, J. Müller, F. Murguia-Flores, V. Naik, Y. Niwa, S. Noce, S. O'Doherty, R. J. Parker, C. Peng, S. Peng, G. P. Peters, C. Prigent, R. Prinn, M. Ramonet, P. Regnier, W. J. Riley, J. A. Rosentreter, A. Segers, I. J. Simpson, H. Shi, S. J. Smith, L. P. Steele, B. F. Thornton, H. Tian, Y. Tohjima, F. N. Tubiello, A. Tsuruta, N. Viovy, A. Voulgarakis, T. S. Weber, M. van Weele, G. R. van der Werf, R. F. Weiss, D. Worthy, D. Wunch, Y. Yin, Y. Yoshida, W. Zhang, Z. Zhang, Y. Zhao, B. Zheng, Q. Zhu, Q. Zhu, Q. Zhuang, The global methane budget, 2000–2017. *Earth Syst. Sci. Data* **12**, 1561–1623 (2020).
6. R. B. Jackson, M. Saunois, P. Bousquet, J. G. Canadell, B. Poulter, A. R. Stavert, P. Bergamaschi, Y. Niwa, A. Segers, A. Tsuruta, Increasing anthropogenic methane emissions arise equally from agricultural and fossil fuel sources. *Environ. Res. Lett.* **15**, 071002 (2020).
7. D. R. Lyon, R. A. Alvarez, D. Zavala-Araiza, A. R. Brandt, R. B. Jackson, S. P. Hamburg, Aerial surveys of elevated hydrocarbon emissions from oil and gas production sites. *Environ. Sci. Technol.* **50**, 4877–4886 (2016).
8. Y. Zhang, R. Gautam, S. Pandey, M. Omara, J. D. Maasakkers, P. Sadavarte, D. Lyon, H. Nesser, M. P. Sulprizio, D. J. Varon, R. Zhang, S. Houweling, D. Zavala-Araiza, R. A. Alvarez, A. Lorente, S. P. Hamburg, I. Aben, D. J. Jacob, Quantifying methane emissions from the largest oil-producing basin in the United States from space. *Sci. Adv.* **6**, eaaz5120 (2020).
9. J. G. Englander, A. R. Brandt, S. Conley, D. R. Lyon, R. B. Jackson, Aerial interyear comparison and quantification of methane emissions persistence in the bakken formation of North Dakota, USA. *Environ. Sci. Technol.* **52**, 8947–8953 (2018).
10. T. N. Lavoie, P. B. Shepson, M. O. L. Cambaliza, B. H. Stirm, A. Karion, C. Sweeney, T. I. Yacovitch, S. C. Herndon, X. Lan, D. Lyon, Aircraft-based measurements of point source methane emissions in the barnett shale basin. *Environ. Sci. Technol.* **49**, 7904–7913 (2015).
11. A. K. Thorpe, C. Frankenberg, D. A. Roberts, Retrieval techniques for airborne imaging of methane concentrations using high spatial and moderate spectral resolution: Application to AVIRIS. *Atmos. Meas. Tech.* **7**, 491–506 (2014).
12. D. R. Thompson, I. Leifer, H. Bovensmann, M. Eastwood, M. Fladeland, C. Frankenberg, K. Gerilowski, R. O. Green, S. Kratwurst, T. Krings, B. Luna, A. K. Thorpe, Real-time remote detection and measurement for airborne imaging spectroscopy: A case study with methane. *Atmos. Meas. Tech.* **8**, 4383–4397 (2015).
13. J. Borchardt, K. Gerilowski, S. Krautwurst, H. Bovensmann, A. K. Thorpe, D. R. Thompson, C. Frankenberg, C. E. Miller, R. M. Duren, J. P. Burrows, Detection and quantification of $CH_4$ plumes using the WFM-DOAS retrieval on AVIRIS-NG hyperspectral data. *Atmos. Meas. Tech. Discuss.* **2020**, 1–34 (2020).
14. C. Frankenberg, A. K. Thorpe, D. R. Thompson, G. Hulley, E. A. Kort, N. Vance, J. Borchardt, T. Krings, K. Gerilowski, C. Sweeney, S. Conley, B. D. Bue, A. D. Aubrey, S. Hook, R. O. Green, Airborne methane remote measurements reveal heavy-tail flux distribution in four corners region. *Proc. Natl. Acad. Sci. U.S.A.* **113**, 9734–9739 (2016).
15. R. Duren, A. K. Thorpe, K. T. Foster, T. Rafiq, F. M. Hopkins, V. Yadav, B. D. Bue, D. R. Thompson, S. Conley, N. K. Colombi, C. Frankenberg, I. B. McCubbin, M. L. Eastwood, M. Falk, J. D. Herner, B. E. Croes, R. O. Green, C. E. Miller, California's methane super-emitters. *Nature* **575**, 180–184 (2019).
16. D. H. Cusworth, R. M. Duren, A. K. Thorpe, E. Tseng, D. Thompson, A. Guha, S. Newman, K. T. Foster, C. E. Miller, Using remote sensing to detect, validate, and quantify methane emissions from california solid waste operations. *Environ. Res. Lett.* **15**, 054012 (2020).
17. D. J. Jacob, A. J. Turner, J. D. Maasakkers, J. Sheng, K. Sun, X. Liu, K. Chance, I. Aben, J. McKeever, C. Frankenberg, Satellite observations of atmospheric methane and their value for quantifying methane emissions. *Atmos. Chem. Phys.* **16**, 14371–14396 (2016).
18. S. Pandey, R. Gautam, S. Houweling, H. D. van der Gon, P. Sadavarte, T. Borsdorff, O. Hasekamp, J. Landgraf, P. Tol, T. van Kempen, R. Hoogeveen, R. van Hees, S. P. Hamburg, J. D. Maasakkers, I. Aben, Satellite observations reveal extreme methane leakage from a natural gas well blowout. *Proc. Natl. Acad. Sci. U.S.A.* **116**, 26376–26381 (2019).
19. J. Barré, I. Aben, A. Agustí-Panareda, G. Balsamo, N. Bousserez, P. Dueben, R. Engelen, A. Inness, A. Lorente, J. McNorton, V.-H. Peuch, G. Radnoti, R. Ribas, Systematic detection of local $CH_4$ emissions anomalies combining satellite measurements and high-resolution forecasts. *Atmos. Chem. Phys. Discuss.* **2020**, 1–25 (2020).
20. O. Schneising, M. Buchwitz, M. Reuter, S. Vanselow, H. Bovensmann, J. P. Burrows, Remote sensing of methane leakage from natural gas and petroleum systems revisited. *Atmos. Chem. Phys.* **20**, 9169–9182 (2020).
21. J. A. de Gouw, J. P. Veefkind, E. Roosenbrand, B. Dix, J. C. Lin, J. Landgraf, P. F. Levelt, Daily satellite observations of methane from oil and gas production regions in the United States. *Sci. Rep.* **10**, 1379 (2020).
22. D. H. Cusworth, D. J. Jacob, J.-X. Sheng, J. Benmergui, A. J. Turner, J. Brandman, L. White, C. A. Randles, Detecting high-emitting methane sources in oil/gas fields using satellite observations. *Atmos. Chem. Phys.* **18**, 16885–16896 (2018).
23. D. H. Cusworth, D. J. Jacob, D. J. Varon, C. Chan Miller, X. Liu, K. Chance, A. K. Thorpe, R. M. Duren, C. E. Miller, D. R. Thompson, C. Frankenberg, L. Guanter, C. A. Randles, Potential of next-generation imaging spectrometers to detect and quantify methane point sources from space. *Atmos. Meas. Tech.* **12**, 5655–5668 (2019).
24. D. R. Thompson, A. K. Thorpe, C. Frankenberg, R. O. Green, R. Duren, L. Guanter, A. Hollstein, E. Middleton, L. Ong, S. Ungar, Space-based remote imaging spectroscopy of the Aliso Canyon $CH_4$ superemitter. *Geophys. Res. Lett.* **43**, 6571–6578 (2016).
25. D. J. Varon, J. McKeever, D. Jervis, J. D. Maasakkers, S. Pandey, S. Houweling, I. Aben, T. Scarpelli, D. J. Jacob, Satellite discovery of anomalously large methane point sources from oil/gas production. *Geophys. Res. Lett.* **46**, 13507–13516 (2019).
26. D. J. Varon, D. J. Jacob, D. Jervis, J. McKeever, Quantifying time-averaged methane emissions from individual coal mine vents with GHGSat-D satellite observations. *Environ. Sci. Technol.* **54**, 10246–10253 (2020).

27. Y.-N. Liu, D.-X. Sun, X.-N. Hu, X. Ye, Y.-D. Li, S.-F. Liu, K.-Q. Cao, M.-Y. Chai, W.-Y.-N. Zhou, J. Zhang, Y. Zhang, W.-W. Sun, L.-L. Jiao, The advanced hyperspectral imager: Aboard China's Gaofen-5 satellite. *IEEE Geosci. Remote Sens. Mag.* **7**, 23–32 (2019).
28. J. D. Maasakkers, D. J. Jacob, M. P. Sulprizio, A. J. Turner, M. Weitz, T. Wirth, C. Hight, M. DeFigueiredo, M. Desai, R. Schmeltz, L. Hockstad, A. A. Bloom, K. W. Bowman, S. Jeong, M. L. Fischer, Gridded national inventory of U.S. methane emissions. *Environ. Sci. Technol.* **50**, 13123–13133 (2016).
29. Enverus DrillingInfo, DI Desktop (2020); http://didesktop.com.
30. A. K. Ayasse, A. K. Thorpe, D. A. Roberts, C. C. Funk, P. E. Dennison, C. Frankenberg, A. Steffke, A. D. Aubrey, Evaluating the effects of surface properties on methane retrievals using a synthetic airborne visible/infrared imaging spectrometer next-generation (AVIRIS-NG) image. *Remote Sens. Environ.* **215**, 386–397 (2018).
31. D. R. Lyon, D. Zavala-Araiza, R. A. Alvarez, R. Harriss, V. Palacios, X. Lan, R. Talbot, T. Lavoie, P. Shepson, T. I. Yacovitch, S. C. Herndon, A. J. Marchese, D. Zimmerle, A. L. Robinson, S. P. Hamburg, Constructing a spatially resolved methane emission inventory for the Barnett Shale region. *Environ. Sci. Technol.* **49**, 8147–8157 (2015).
32. D. Zavala-Araiza, R. Alvarez, D. Lyon, D. Allen, A. Marchese, D. Zimmerle, S. Hamburg, Superemitters in natural gas infrastructure are caused by abnormal process conditions. *Nat. Commun.* **8**, 14012 (2017).
33. A. R. Brandt, G. A. Heath, D. Cooley, Methane leaks from natural gas systems follow extreme distributions. *Environ. Sci. Technol.* **50**, 12512–12520 (2016).
34. S. S. Kumar, J. Hult, J. Picotte, B. Peterson, Potential underestimation of satellite fire radiative power retrievals over gas flares and wildland fires. *Remote Sens.* **12**, 238 (2020).
35. A. Gvakharia, E. A. Kort, A. Brandt, J. Peischl, T. B. Ryerson, J. P. Schwarz, M. L. Smith, C. Sweeney, Methane, black carbon, and ethane emissions from natural gas flares in the bakken shale, North Dakota. *Environ. Sci. Technol.* **51**, 5317–5325 (2017).
36. H. Tabuchi, A secret recording reveals oil executives' private views on climate change, *New York Times*, 2020.
37. L. Guanter, H. Kaufmann, K. Segl, S. Foerster, C. Rogass, S. Chabrillat, T. Kuester, A. Hollstein, G. Rossner, C. Chlebek, C. Straif, S. Fischer, S. Schrader, T. Storch, U. Heiden, A. Mueller, M. Bachmann, H. Mühle, R. Müller, M. Habermeyer, A. Ohndorf, J. Hill, H. Buddenbaum, P. Hostert, S. van der Linden, P. Leitão, A. Rabe, R. Doerffer, H. Krasemann, H. Xi, W. Mauser, T. Hank, M. Locherer, M. Rast, K. Staenz, B. Sang, The EnMAP spaceborne imaging spectroscopy mission for earth observation. *Remote Sens.* **7**, 8830–8857 (2015).
38. D. J. Varon, D. Jervis, J. McKeever, I. Spence, D. Gains, D. J. Jacob, High-frequency monitoring of anomalous methane point sources with multispectral Sentinel-2 satellite observations. *Atmos. Meas. Tech. Discuss.* **2020**, 1–21 (2020).
39. D. R. Lyon, B. Hmiel, R. Gautam, M. Omara, K. Roberts, Z. R. Barkley, K. J. David, N. L. Miles, V. C. Monteiro, S. J. Richardson, S. Conley, M. L. Smith, D. J. Jacob, L. Shen, D. J. Varon, A. Deng, X. Rudelis, N. Sharma, K. T. Story, A. R. Brandt, M. Kang, E. A. Kort, A. J. Marchese, S. P. Hamburg, Concurrent variation in oil and gas methane emissions and oil price during the COVID-19 pandemic. *Atmos. Chem. Phys. Discuss.* **21**, 6605–6626 (2021).
40. United States Environmental Protection Agency, EPA Issues Final Policy and Technical Amendments to the New Source Performance Standards for the Oil and Natural Gas Industry (2020); https:// epa.gov/controlling-air-pollution-oil-and-natural-gas-industry/epa-issues-final-policy-and-technical.
41. M. D. Foote, P. E. Dennison, A. K. Thorpe, D. R. Thompson, S. Jongaramrungruang, C. Frankenberg, S. C. Joshi, Fast and accurate retrieval of methane concentration from imaging spectrometer data using sparsity prior. *IEEE Trans. Geosci. Remote Sens.* **58**, 6480–6492 (2020).
42. D. J. Varon, D. J. Jacob, J. McKeever, D. Jervis, B. O. A. Durak, Y. Xia, Y. Huang, Quantifying methane point sources from fine-scale satellite observations of atmospheric methane plumes. *Atmos. Meas. Tech.* **11**, 5673–5686 (2018).
43. T. Lauvaux, A. E. Schuh, M. Uliasz, S. Richardson, N. Miles, A. E. Andrews, C. Sweeney, L. I. Diaz, D. Martins, P. B. Shepson, K. J. Davis, Constraining the $CO_2$ budget of the corn belt: Exploring uncertainties from the assumptions in a mesoscale inverse system. *Atmos. Chem. Phys.* **12**, 337–354 (2012).
44. PermianMAP (Methane Analysis Project) (2020); https://data.permianmap.org/pages/operators.
45. Railroad Commission of Texas (2020); https://rrc.state.tx.us/about-us/resource-center/research/data-sets-available-for-download/.
46. New Mexico Department of Energy, Minerals, and Natural Resources (2020); http://emnrd.state.nm.us/OCD/ocdgis.html.


**Acknowledgments:** We thank R. Colombo from the University of Milano—Bicocca (Italy) for initial assistance to request PRISMA data. **Funding:** I.I.-L., L.G., J.G., and E.S.-G. are partly funded by an UPV-GFZ Potsdam EnMAP collaboration contract. Yuzhong Zhang is funded by the National Natural Science Foundation of China (project 42007198) and foundation of Westlake University. **Author contributions:** Conceptualization and methodology: L.G. and I.I.-L.; formal analysis: I.I.-L., L.G., D.J.V., J.D.M., Yu. Z., A.C., S.C.W., A.K.T., R.M.D., D.H.C., K.S., J.G., and E.S.-G.; investigation: all authors; resources: Y.-N.L., A.C., S.C.W., Yo. Z., K.C., H.Z., J.L., and M.P.S.; supervision: L.G., C.F., D.J.J., D.R.L., and I.A.; writing—original draft: L.G.; writing—review and editing: all authors. **Competing interests:** The authors declare that they have no competing interests. **Data and materials availability:** Images of the detected plumes overlaid onto high-resolution images can be accessed through the online Geographic Information System https://qgiscloud.com/Itziar_Irakulis/PERMIAN_CH4_MAP_LARS/. All data needed to evaluate the conclusions in the paper are present in the paper and/or the Supplementary Materials. The raw methane plume datasets used in this analysis can be found in https://doi.org/10.7910/DVN/K8SN73.

Submitted 27 October 2020
Accepted 13 May 2021
Published 30 June 2021
10.1126/sciadv.abf4507

**Citation:** I. Irakulis-Loitxate, L. Guanter, Y.-N. Liu, D. J. Varon, J. D. Maasakkers, Y. Zhang, A. Chulakadabba, S. C. Wofsy, A. K. Thorpe, R. M. Duren, C. Frankenberg, D. R. Lyon, B. Hmiel, D. H. Cusworth, Y. Zhang, K. Segl, J. Gorroño, E. Sánchez-García, M. P. Sulprizio, K. Cao, H. Zhu, J. Liang, X. Li, I. Aben, D. J. Jacob, Satellite-based survey of extreme methane emissions in the Permian basin. *Sci. Adv.* **7**, eabf4507 (2021).

# Satellite-based survey of extreme methane emissions in the Permian basin

Itziar Irakulis-Loitxate, Luis Guanter, Yin-Nian Liu, Daniel J. Varon, Joannes D. Maasakkers, Yuzhong Zhang, Apisada Chulakadabba, Steven C. Wofsy, Andrew K. Thorpe, Riley M. Duren, Christian Frankenberg, David R. Lyon, Benjamin Hmiel, Daniel H. Cusworth, Yongguang Zhang, Karl Segl, Javier Gorroño, Elena Sánchez-García, Melissa P. Sulprizio, Kaiqin Cao, Haijian Zhu, Jian Liang, Xun Li, Ilse Aben and Daniel J. Jacob

*Sci Adv* **7** (27), eabf4507.
DOI: 10.1126/sciadv.abf4507